AGU PUBLICATIONS

JGR

Journal of Geophysical Research: Solid Earth

RESEARCH ARTICLE
10.1002/2015JB012427

This article is a companion to *Ye et al.* [2016] doi:10.1002/2015JB012426.

Key Points:
- Source parameters for 114 major megathrust ruptures are examined for depth dependence
- Shallow events, including tsunami earthquakes, have low stress drop and apparent stress
- The relative amount of high-frequency energy increases with source depth but not total energy

Supporting Information:
- Figures S1 and S2 and Text S1
- Figures S3–S36

Correspondence to:
T. Lay,
tlay@ucsc.edu

Citation:
Ye, L., T. Lay, H. Kanamori, and L. Rivera (2016), Rupture characteristics of major and great ($M_w \geq 7.0$) megathrust earthquakes from 1990 to 2015: 2. Depth dependence, *J. Geophys. Res. Solid Earth*, *121*, doi:10.1002/2015JB012427.

Received 6 AUG 2015
Accepted 6 JAN 2016
Accepted article online 11 JAN 2016

Rupture characteristics of major and great ($M_w \geq 7.0$) megathrust earthquakes from 1990 to 2015: 2. Depth dependence

Lingling Ye[1,2], Thorne Lay[1], Hiroo Kanamori[2], and Luis Rivera[3]

[1]Department of Earth and Planetary Sciences, University of California, Santa Cruz, California, USA, [2]Seismological Laboratory, California Institute of Technology, Pasadena, California, USA, [3]Institut de Physique du Globe de Strasbourg (UMR7516), Université de Strasbourg/CNRS, Strasbourg, France

Abstract Depth-varying characteristics of high-frequency seismic radiation for megathrust earthquakes have been inferred from several recent giant earthquakes and large tsunami earthquakes. To quantify any depth dependence more extensively, we analyzed 114 $M_w \geq 7.0$ thrust-faulting earthquakes with centroid depths from 5 to 55 km on circum-Pacific megathrusts using teleseismic body wave finite-fault inversions and source spectrum determinations. Large tsunami earthquakes and some other shallow events at depths less than about 18 km have unusually long source durations, and low values of static stress drop ($\Delta\sigma_E$), $V_r^3\Delta\sigma_E$, and apparent stress, with relatively depleted high-frequency radiation. Deeper events have no clear global trend with source depth for moment-normalized centroid time or total duration, static stress drop, moment-scaled radiated energy, apparent stress, or radiation efficiency. Regional behavior among the 17 sampled subduction zones generally conforms to the global composite. The source spectra have high-frequency logarithmic spectral decay slopes averaging ~ −1.6. There is relative enrichment in high-frequency spectral levels with increasing source depth manifested in reduced high-frequency spectral decay slope. The ratio of high-frequency (0.3–1 Hz) radiated energy to total energy increases correspondingly. These observations suggest that overall dynamic rupture processes are relatively insensitive to source depth, but varying scale lengths of megathrust heterogeneity may contribute to modest enrichment of high-frequency seismic radiation for events deeper on the megathrust. A weak correlation of higher estimated average megathrust temperature at 30 km depth with higher spectral decay rate indicates that the depth-varying pattern may in part result from frictional properties being influenced by temperature variations or by systematic reduction of average attenuation with increasing depth along the megathrust.

1. Introduction

Devastating tsunami and strong ground shaking are two principal hazards from large earthquakes located in subduction zones [e.g., *Kanamori*, 2014]. Motivated by recent occurrence of several giant earthquakes and large tsunami earthquakes, along with improved resolution of finite-fault slip distributions from inversions of seismic and geodetic observations and new backprojection methods for imaging coherent high-frequency (HF) radiation from the rupture area, *Lay et al.* [2012] proposed the conceptual model for megathrust ruptures shown in Figure 1. They introduced depth-varying domains A, B, C, and D with distinct seismic radiation characteristics that provide a general framework for considering hazards for large interplate events. There is very little high frequency seismic radiation but strong tsunami excitation from the shallowest domain A, where tsunami earthquakes and some slow slip events occur. Modest levels of spatially distributed high-frequency radiation and large slip are typical for the central domain B, where most megathrust events occur. Concentrated bursts of high-frequency radiation during domain C events at depths of 30–50 km accentuate strong ground-shaking hazard from the deeper ruptures. Domain D represents a transition at the deep edge of the seismogenic zone, observed only in some regions, with diverse occurrence of slow slip events, low-frequency earthquakes, and/or seismic tremor.

A few tests of this conceptual model using teleseismic and regional spectral estimates have been applied to events in individual subduction zones along the Japan Trench offshore of Honshu [*Ye et al.*, 2013a] and along the Middle American Trench [*Ye et al.*, 2013b; *Geirsson et al.*, 2015], yielding general support for depth dependence of some aspects of megathrust ruptures. Isolation of the source spectra for magnitude 6.0–7.6 events offshore Honshu with an empirical Green's function (EGF) method for regional network observations

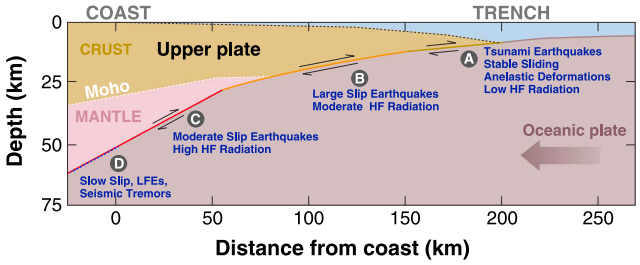

Figure 1. Schematic cross section of a generic interplate subduction zone megathrust fault with four domains of depth-varying rupture characteristics: A, near-trench domain where either low radiated energy tsunami earthquakes occur or anelastic deformation and stable sliding accommodate interplate deformation; B, central megathrust domain where large coseismic slip occurs with moderate high-frequency (HF) seismic radiation; C, downdip domain where moderate coseismic slip occurs with relatively enhanced levels of high-frequency seismic radiation; and D, transitional domain, only present in some areas, typically those with a young subducting plate, where slow slip events, low-frequency earthquakes (LFEs), and seismic tremor occur. (Modified from *Lay et al.* [2012] and *Kanamori* [2014]).

in Japan demonstrated that both depth-varying source radiation and path attenuation variations account for observed ground-shaking patterns [*Ye et al.*, 2013a]. Studies such as *Choy et al.* [2006], *Venkataraman and Kanamori* [2004], and *Ye et al.* [2012a, 2012b, 2013a, 2013b] have demonstrated the distinct seismic radiation characteristics of off-megathrust intraplate faulting, both for outer trench slope faulting and intraslab faulting downdip of the megathrust. Thus, careful identification of megathrust events is required. It is still challenging to seek any depth-varying rupture characteristics for confidently identified events on global subduction zone megathrusts due to limited availability of regional broadband observations and because earthquakes are intrinsically diverse, with substantial variability in rupture processes and strong along-strike variations [*El Hariri et al.*, 2013; *Ye et al.*, 2012a, 2013b]. Fortunately, *Ye et al.* [2013a] found good consistency in overall characteristics of teleseismic and regional EGF-corrected source spectra, giving confidence that teleseismic estimates can provide reliable relative source characteristics up to 1–2 Hz. Building on that study, we systematically analyze source characteristics using teleseismic data for large interplate earthquakes in global subduction zones.

The data set used in this study is the same as in *Ye et al.* [2016: henceforth called Paper 1]. Paper 1 focuses on scaling relationships for various source parameters of major and great interplate earthquakes. We use the same measurements for 114 $M_w \geq 7$ earthquakes from 1990 to 2015 (Figure 2), identified as megathrust ruptures based on their locations, source depths (from ~5 km to 55 km), and focal mechanisms. All of the measurements and finite-fault inversions use only global broadband body wave observations for frequencies below 1–2 Hz. This paper focuses on the faulting characteristics in the context of tectonic environment and source depth, drawing upon the scaling relations established in Paper 1. Given the intrinsic limitations of source parameter estimates inferred from finite-fault inversions that use only teleseismic data and far-field source spectrum estimates and the variety of subduction zone environments in which the earthquakes occur, large scatter is expected. We seek any underlying systematic behavior that can be confidently resolved. It is just as important to document any lack of depth dependence of source behavior as any systematic change with source depth.

Due to the strong trade-off between estimated static stress drop and assumed rupture expansion velocity (V_r) for time domain finite-fault inversions using only teleseismic data, we follow Paper 1 in subdividing all events into either group 1 (18 events) having independent constraints on V_r from prior studies or group 2 (96 events) lacking independent V_r constraints. For group 2, finite-fault inversions with $V_r = 2.0$, 2.5, and 3.0 km/s were performed. Details of the data selection and finite-fault inversions are presented in Paper 1, and a link to digital information is given in the acknowledgment. Figure 3 shows three examples of finite-fault models for earthquakes at various depths. Text S1 in the supporting information displays all the finite-fault solutions for group 1 and $V_r = 2.5$ km/s models for group 2 on regional maps for the 17 subduction zones sampled by our events. For each event we determined the moment rate function from finite-fault inversions of teleseismic body waves filtered in the frequency band 0.005–0.9 Hz, the average focal mechanism from planar fault models with variable subfault rake, the space-time slip distribution and subfault source time functions parameterized by multiple overlapping triangular subevents, and the shear stress distribution for the final slip model. For these finite-fault rupture solutions, we computed the seismic moment (M_0), rupture centroid depth (H_c) estimated by average depth of the slip distribution, and averages of source rigidity (μ), *P* wave velocity (V_p), *S* wave velocity (V_s), and density (ρ) over the slip distribution. The source centroid time (T_c)

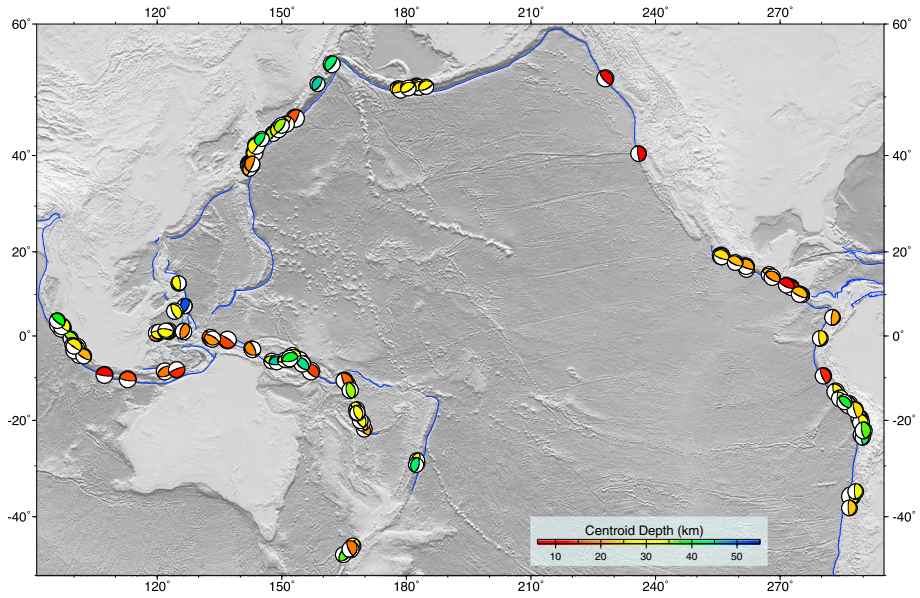

Figure 2. Epicentral locations indicated by best double-couple focal mechanisms from the Global Centroid Moment Tensor (GCMT) catalog for the 114 major and great ($M_w \geq 7$) megathrust earthquakes from 1990 to 2015 analyzed in this study. Focal mechanism radius is scaled proportional to M_w, and color indicates GCMT centroid depth. All major and great interplate thrust events for which reliable source parameter estimates could be made are included.

and total duration (T_d) measured from the origin time are determined from the corresponding moment rate function. Average static stress drop ($\Delta\sigma_E$) weighted by the slip distribution is computed following the method of *Noda et al*. [2013]. In Paper 1 summary rupture parameters for all of the finite-fault models were evaluated by comparing the seismic moment, centroid time and centroid source depths with corresponding values from the Global Centroid Moment Tensor (GCMT) catalog (http://www.globalcmt.org/CMTsearch.html) [*Ekström et al*., 2012], and *W* phase inversions [*Duputel et al*., 2013]. Given the spatial finiteness of the large earthquakes considered, we use the average source depths, with ±5 km uncertainty, rather than hypocentral depths, when examining depth-varying characteristics in this paper. The actual average slip versus depth distribution for each rupture model is displayed in Text S1.

2. Source Duration and Static Stress Drop

2.1. Source Duration

Earthquake characteristic source duration, τ, (parameterized by either source duration T_d or centroid time T_c in our measurements) generally scales with seismic moment, M_0, and other source parameters by

$$\frac{\tau}{(M_0)^{1/3}} \propto \frac{\tau}{\left(L^3 \cdot \Delta\sigma\right)^{1/3}} \propto \frac{1}{V_r \Delta\sigma^{1/3}}, \tag{1}$$

where L is a general rupture dimension, V_r is the rupture velocity, and $\Delta\sigma$ is the static stress drop. This assumes a simple rupture expansion and that width scales with L. Paper 1 confirmed the dominance of cube root scaling of seismic moment for both characteristic source time measurements for our events, with little dependence on parameters used in obtaining the corresponding finite-fault models. Figure 4a shows the moment-scaled centroid time, $T_c^N = T_c \times (M_{0\mathrm{ref}}/M_0)^{1/3}$, where $M_{0\mathrm{ref}}$ is 1.16×10^{18} N m ($M_w \sim 6$) and centroid time T_c is measured from the moment rate function of our finite-fault models. The average moment-scaled centroid time for all 114 great and major events is ~2.9 s. It is ~2.8 s if we exclude the five labeled tsunami earthquakes [*Polet and Kanamori*, 2009]. There is no significant depth variation in the moment-scaled centroid time estimations, T_c^N, apart from the shallow tsunami earthquake behavior (Figure 4a). The 15 August 2007 M_w 8.0 Pisco, Peru earthquake stands out with a significantly long centroid time due to its compound rupture process with a ~60 s hiatus in the seismic radiation between doublet events [*Lay et al*., 2010]. The centroid times are quite robust estimates, with little influence of model assumptions.

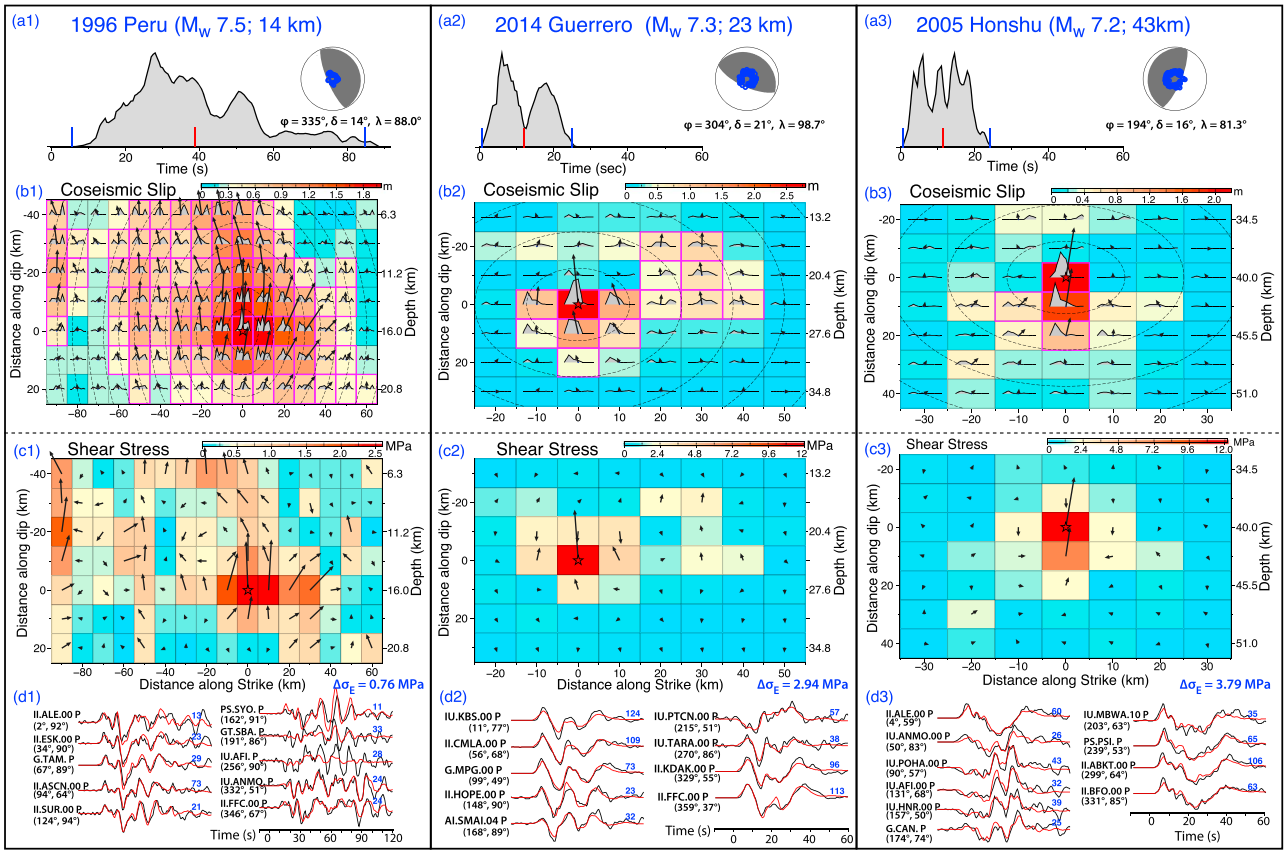

Figure 3. For each event in Figure 2, a finite-source model has been determined by linear least squares inversion of teleseismic *P* (and in some cases *SH*) waves. Representative examples of finite-fault inversions are shown for the (1) 21 February 1996 Peru event (M_w 7.5), (2) 18 April 2014 Guerrero, Mexico event (M_w 7.3), and (3) 16 August 2005 Japan event (M_w 7.2). Solution parameters are listed in Table S1. (a) The moment rate function for each inversion. Blue ticks indicate the time span used to determine total duration, T_d, and the centroid time, T_c, is indicated by the red tick. The average focal mechanism with double-couple strike (ϕ), dip (δ), and rake (λ) is almost identical for each inversion with different V_r. (b) The subfault grid, with average subfault slip direction and magnitude indicated by the vectors, and slip magnitude color coded. Dashed circles indicated rupture front position in 5 s intervals. (c) The average stress vector at the center of each subfault used to compute stress drop for the variable slip solution. (d) Example waveform fits (data are black, and model predictions are red). Below each station name the azimuth and distance of the station relative to the source are indicated. The peak-to-peak amplitude of the data trace in microns is shown in blue; each waveform is normalized to uniform amplitude.

The total source duration measure, T_d, is a somewhat more uncertain parameter, as it is influenced by the inadequacy of the Green's functions for accounting for water reverberations and late scattered waves. We obtained T_d estimates by eye in *Paper I*, ignoring very weak tails in our moment rate functions, as these may be artifacts due to inaccurate modeling of the coda, but the nature of the inversions with positivity constraint is such that these measurements may still be biased a bit long. In Figure 4b we combine our large event T_d measurements with corresponding source duration measurements for smaller events from *Bilek et al*. [2012] and *El Hariri et al*. [2013]. The latter two studies estimated source duration from point source moment rate functions obtained by simultaneous deconvolution of teleseismic broadband *P* wave recordings without positivity constraint for 613 globally distributed interplate thrusting events with $M_w = 5.0–7.0$.

The T_d values in Figure 4b are again scaled by $M_0^{1/3}$ relative to the reference $M_{0\mathrm{ref}} = 1.122 \times 10^{18}$ N m and show similar behavior with source depth to that for centroid times (Figure 4a). Here the preferred point source depths for the simultaneous deconvolutions [*Bilek et al*., 2012; *El Hariri et al*., 2013] are used for the smaller events. There is a greater spread in moment-scaled T_d estimates for depths less than about 18 km (~15 km below the seafloor, assuming there is on average about 3 km of water above the subduction zone). While some of these are large tsunami earthquakes, others are smaller events that were not particularly tsunamigenic but do have very long scaled source durations. This shallow depth range corresponds to domain A in the model of *Lay et al*. [2012] (Figure 1).

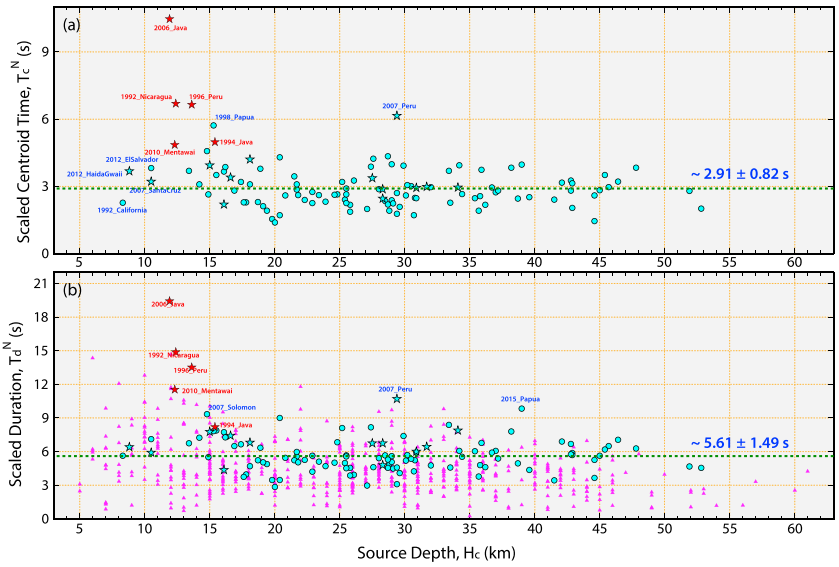

Figure 4. The moment-scaled estimates of (a) the centroid time, T_c^N and (b) the source duration, T_d^N, by cube root scaling of seismic moment relative to a reference seismic moment $M_{ref} = 1.122 \times 10^{18}$ N m ($M_w \sim 6$). Circles (group 2 events) and stars (group 1 events) in Figures 4a and 4b are results from this study, with source duration estimated from the moment rate function and average source depth from the slip distribution of finite-fault inversions. Triangles in Figure 4b are results for 613 events (M_w 5–7) between 1989 and 2011 from *Bilek et al.* [2012] and *El Hariri et al.* [2013] with source duration and depth estimated by point source simultaneous deconvolution of teleseismic broadband *P* wave recordings. The horizontal dashed lines in Figures 4a and 4b indicate the average values of ~2.9 s and ~5.6 s for the moment-scaled durations and centroid times in this study, respectively. In Figures 4a and 4b the measures for large tsunami earthquakes are labeled in red, and some events with anomalous long duration/centroid times are labeled in blue, like the 15 August 2007 M_w 8.0 Peru and 2007 M_w 7.9 Sumatra doublet events.

There is no clear trend for either moment-scaled T_d or moment-scaled T_c for depths larger than 18 km. The average moment-scaled T_d for our large events is ~8.0 s for 24 events with depths less than 18 km, ~5.4 s for 90 events with larger depths, and ~6.0 s overall (or ~5.6 s excluding the five tsunami earthquakes). The average moment-scaled T_c is ~4.1 s and ~2.8 s for the shallower and deeper event populations, respectively, which is consistent with the factor of slightly less than 2 ratio of T_d/T_c expected for the typical asymmetric triangular shapes of the moment rate functions. For the population of events with $M_w < 7.0$ from *El Hariri et al.* [2013] and *Bilek et al.* [2012], the average moment-scaled T_d for all 123 shallower (<18 km) events is ~5.5 s and for 490 deeper (18–60 km) events it is ~4.3 s, both of which are shorter than our finite faulting-based durations. Our inclusion of large tsunami earthquakes affects the shallower distribution. The difference for deeper events may be due to intrinsic differences in estimating the total duration from simultaneously deconvolved point source source time functions without positivity constraint versus our estimates from moment rate functions for finite-fault inversions with a positivity constraint or it may reflect differences in signal-to-noise ratios between the populations.

The composite behavior of duration measures versus source depth is similarly reflected in the individual subduction zones. Plots of moment-scaled T_c versus depth for events in the 17 sampled subduction zones are shown for each region in Text S1. Some regions have few major and great earthquakes, but others have moderate numbers allowing any local trends to be detected. The regional plots do not reveal any distinct behavior from the global composite in Figure 4.

2.2. Static Stress Drop

The average static stress drop, proportional to the ratio of coseismic slip to a characteristic rupture dimension, is an important measure of the change of stress level on the fault due to the earthquake rupture process. There is large estimation uncertainty for stress drop due to limited resolution of rupture finiteness from teleseismic data only. This issue is extensively addressed in Paper 1, and the energy-related stress drop $\Delta\sigma_E$, given by the spatial average of the stress drop weighted by slip [*Noda et al.*, 2013; *Ye et al.*, 2013c], is preferred as a

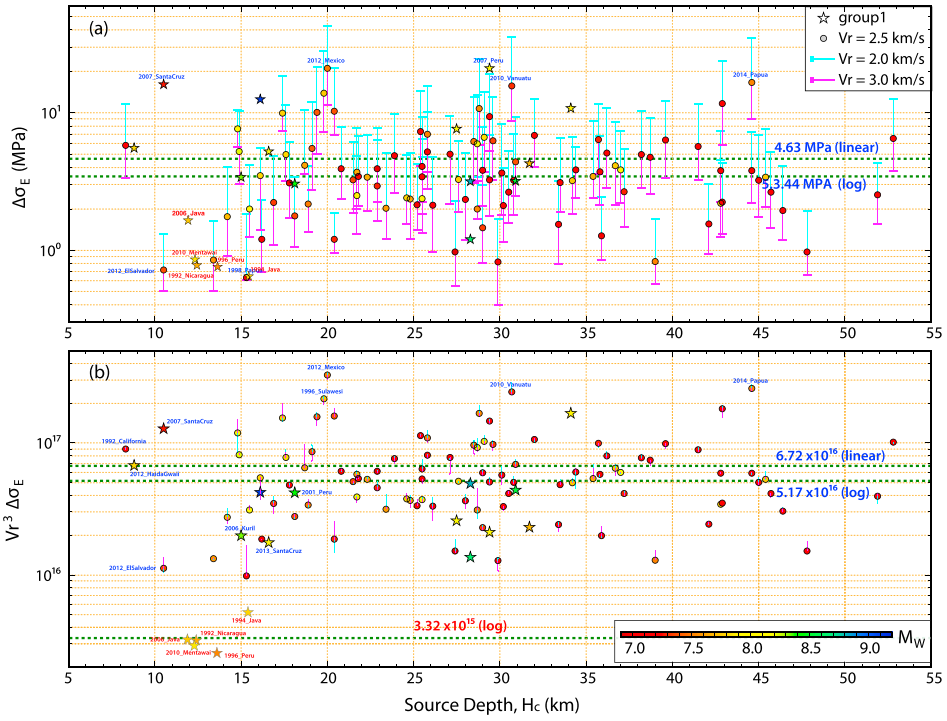

Figure 5. The ranges of (a) stress drop, $\Delta\sigma_E$, and (b) the product of $V_r^3\Delta\sigma_E$, plotted versus average depth of the slip distribution from the finite-fault inversion. The stress drop, $\Delta\sigma_E$, is calculated from variable slip finite-source models with $V_r = 2.0$ km/s (upper cyan estimates) to $V_r = 2.5$ km/s (circles) to $V_r = 3.0$ km/s (lower magenta estimates). The stars are for group 1 finite-fault models with independent estimates of V_r. Events with high or low values are labeled. Tsunami earthquakes are highlighted with red text. The symbol colors denote M_w. The linear and log averages of the entire population are indicated by the labeled green dashed lines.

relatively robust stress drop measurement. $\Delta\sigma_E$ still varies systematically with rupture expansion velocity used in our finite-fault inversions for group 2 events (Table 2 in Paper 1).

Figure 5a shows that there is no systematic global variation in stress drop $\Delta\sigma_E$ for the range of finite-fault inversions performed for each event in group 2 as a function of source depth H_c. The overall average static stress drop is ~4 MPa for all 114 M_w 7–9 earthquakes we analyzed, with the estimates spanning values from ~0.4 MPa to ~40 MPa. Paper 1 demonstrated that $\Delta\sigma_E$ does not have systematic magnitude dependence either. The variation in $\Delta\sigma_E$ is largest among earthquakes with depths less than 18 km, and large tsunami earthquakes have relatively low values. However, the pattern is not as systematic or distinct as found for the duration estimates (Figure 4) as there are comparably low stress drop events deeper on the megathrust as well as ordinary stress drop shallow events. The large stress drop for the 2 September 2007 M_w 7.3 Santa Cruz event is uncertain due to difficulty in modeling strong *P* coda reverberations at some azimuths. The 28 October 2012 Haida Gwaii M_w 7.8 earthquake, with a stress drop of ~5 MPa, is well constrained to have shallow depth by both seismic and tsunami modeling [*Lay et al.*, 2013b] and has a rupture velocity of 2.3 km/s, significantly larger than that for comparably shallow tsunami events; thus, the variability at shallow depth appears to be real.

Examination of $\Delta\sigma_E$ versus H_c for each of the 17 subduction zones separately (Text S1) shows general similarity with the composite behavior in Figure 5a. Central America displays a trend of increasing stress drop with depth from 10 to 30 km, but the scatter is too large or the number of data is too small to resolve depth dependence in any of the other regions. We do not detect significant baseline shifts in stress drop between regions either. Detailed analysis of larger numbers of events in each region, including smaller events, is warranted, but our large events do not indicate strong regional patterns.

In Paper 1, it was established that the product $V_r^3\Delta\sigma_E$ is very stable for each event across the suite of models with V_r ranging from 2 to 3 km/s. It is appealing to explore this parameter, as it is relatively free of modeling assumptions. Figure 5b shows that $V_r^3\Delta\sigma_E$ has a pattern with source depth opposite to that for the duration

estimates, consistent with equation (1). The low rupture velocity tsunami earthquakes are well isolated from the other events with average values about a factor of 20 lower than the overall population. The behavior appears to be either a step change or a rapidly increasing trend for source depths from 5 to ~18 km, although events like 2012 Haida Gwaii deviate from either pattern.

3. Far-Field Source Spectrum Analysis

To investigate frequency-dependent seismic radiation characteristics across the megathrust, we evaluate whether there is any variation with source depth in high-frequency spectral decay, moment-scaled radiated energy, or apparent stress parameters for the 114 $M_w \geq 7$ interplate thrust events.

The moment rate spectrum $\left(\hat{\dot{M}}(f)\right)$, or source spectrum, at frequencies higher than 0.05 Hz in this study is obtained from the observed ground displacement spectrum ($\hat{u}(f)$) at a station by

$$\left|\hat{\dot{M}}(f)\right| = \frac{4\pi\rho_h V_{\alpha,\beta}^3 R_E}{g(\Delta)R(\theta,\phi)} \cdot \frac{|\hat{u}(f)|}{C\left|\hat{I}(f)\right|} \cdot e^{-\pi f t^*}, \tag{2}$$

where $V_{\alpha,\beta}$ and ρ_h are the *P* wave or *S* wave velocity and density at the source region, $R_E = 6371$ km is the radius of the earth, $g(\Delta)/R_E$ is the geometric spreading for each path at teleseismic distances, *C* is the free surface receiver effect, and $\hat{I}(f)$ is the instrumental response. t^* is the attenuation factor (equal to the travel time divided by the path-averaged *Q* factor); we use the attenuation model from *Pérez-Campos et al.* [2003], with t^* reducing with increasing frequency, as determined by reconciling teleseismic and regional estimates of seismic energy. $R(\theta,\phi)$ is the average radiation pattern for *P*, *pP*, and *sP* phases for the final average focal mechanism and centroid source depth from the finite-fault inversions. Because the depth phases are difficult to separate for large shallow earthquakes, we applied the combined correction for the *P*, *pP*, and *sP* phase amplitudes formulated by *Boatwright and Choy* [1986]. These corrections are appropriate only for frequencies above ~0.05 Hz. To obtain the average source spectrum for frequencies above 0.05 Hz, we logarithmically average the individual-corrected moment rate spectra from (2) for stations with good azimuthal coverage and stable radiation pattern coefficients.

To estimate the source spectra at frequencies lower than 0.05 Hz, we use the spectra computed from the moment rate functions obtained by the finite-fault inversions of teleseismic body waves. We normalize the low-frequency level to the long-period GCMT seismic moment.

We combine the source spectra from the finite-fault moment rate functions and from the average *P* wave observations to obtain broadband source spectra for frequencies up to about 1–2 Hz. In most cases, the spectral estimates are consistent in the vicinity of the cross-over frequency of 0.05 Hz. The gray curves in Figure 6 show representative source spectra thus computed for the 21 February 1996 Peru, 18 April 2014 Guerrero, and 16 August 2005 Honshu earthquakes. These are typical of the source spectra for major and large events in the shallow domain A, domain B, and deep domain C regions, respectively. There is some spectral notching structure near the corner frequency for each event, with a relatively stable low-frequency level and smoothly decaying spectrum above 0.1 Hz. The notches in the spectra are real source characteristics. The source spectra for all events are shown in Text S1, grouped by subduction zone.

We fit each average far-field source spectrum by a spectrum, ω^{-n_0}, given by

$$\left|\hat{\dot{M}}(f; M_0, f_c, n_0)\right| = \frac{M_0}{1 + (f/f_c)^{n_0}}, \tag{3}$$

where M_0 is the seismic moment, f_c is the corner frequency, and n_0 is a constant that determines the high-frequency falloff. This form is similar to that of the standard *Brune* [1970] ω^{-2} spectrum, but we allow a more general spectral decay rate. We determined f_c and n_0 by minimizing the difference between the predicted moment rate spectrum given by equation (3) and the observed spectrum. We use the seismic moment M_0 from the GCMT catalog, which is consistent with our finite-fault inversion solutions. The frequency band used for the spectral fitting is from 0 Hz to a high-frequency cutoff about 25 times the corner frequency, but 1 Hz is used as an upper limit for smaller events with large corner frequency. The red curves in Figure 6 shows the best-fitting ω^{-n_0} model for the 21 February 1996 Peru, 18 April 2014 M_w 7.3 Guerrero, and 16 August 2005

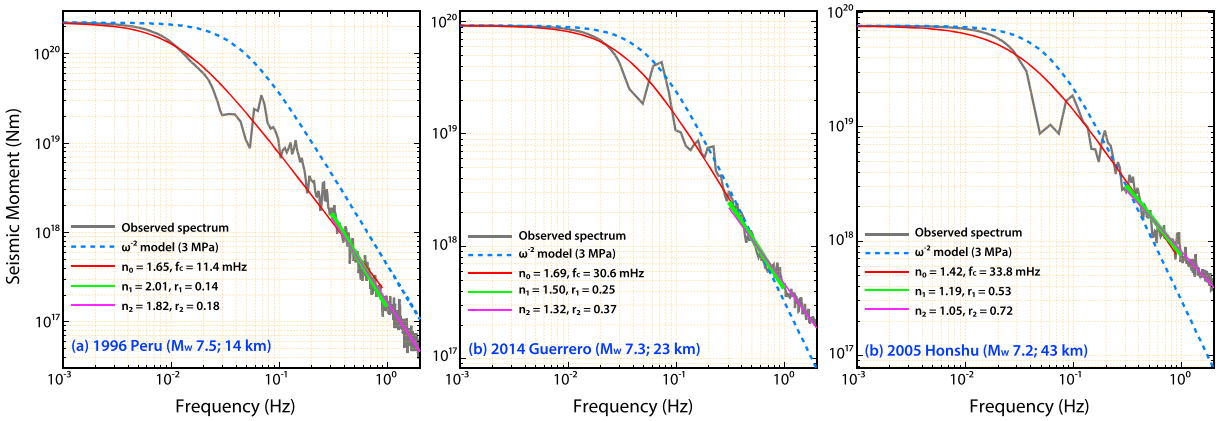

Figure 6. For each event in Figure 2 an average source spectrum was estimated, and various parameters were measured to characterize the shape of the spectrum. Representative examples are shown (gray lines) for the (a) 21 February 1996 Peru event (M_w 7.5); (b) 18 April 2014 Guerrero, Mexico event (M_w 7.3); and (c) 16 August 2005 Japan event (M_w 7.2). The source spectra for frequencies less than ~0.05 Hz are from the moment rate function of the finite-fault model inversion of teleseismic *P* wave observations (Figure 3), and for frequencies higher than ~0.05 Hz the spectrum is calculated by averaging broadband teleseismic *P* wave spectra corrected for an attenuation model, radiation pattern, and geometric spreading. The blue dash lines are the reference source spectra for ω^{-2} model with 3 MPa stress parameter, shear velocity 3.75 km/s, and seismic moments from GCMT solutions. The red lines are best-fitting ω^{-n_0} model with optimized corner frequency (f_c) and high-frequency fall-off rate (n_0). The green and magenta lines show linear regressions for slope of the high-frequency spectrum from 0.3 to 1.0 Hz and 0.3 to 2.0 Hz with slopes of n_1 and n_2, respectively.

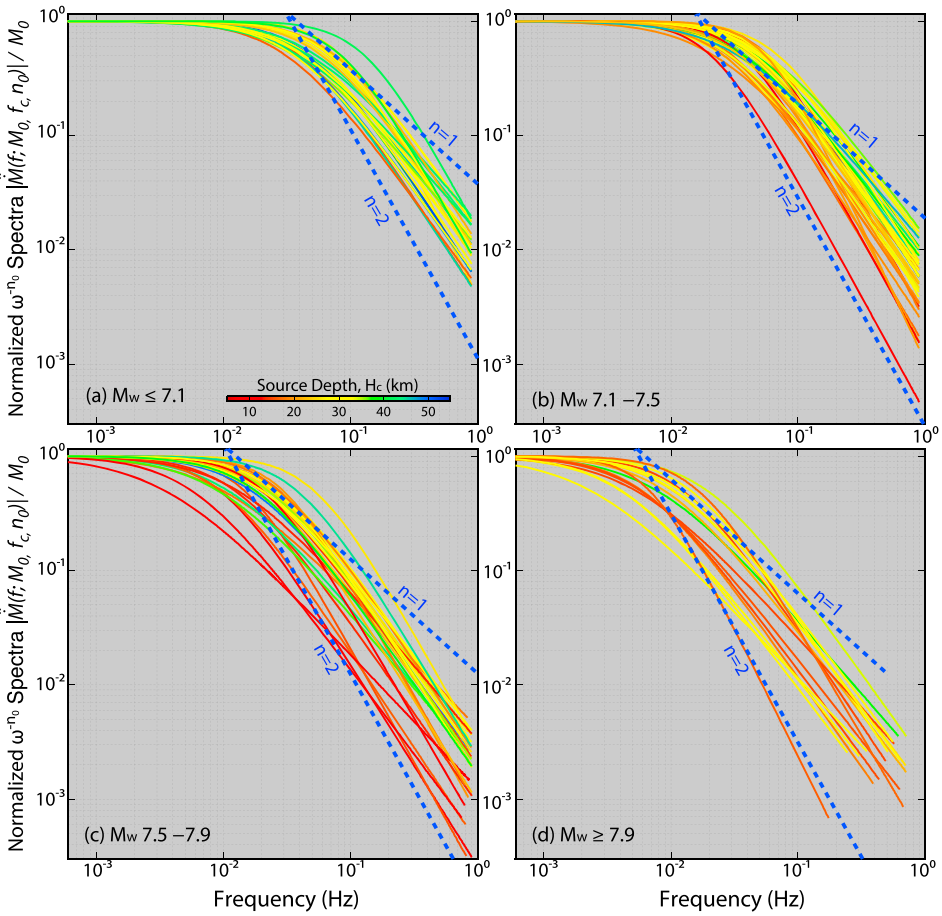

Figure 7. The best-fitting ω^{-n_0} models for events with (a) $M_w < 7.1$, (b) M_w 7.1–7.5, (c) M_w 7.5–7.9, and (d) $M_w > 7.9$. Two blue dashed straight lines in each panel indicate reference high-frequency decay slopes of 1 and 2. Colors indicate average depth of the slip distribution for each event.

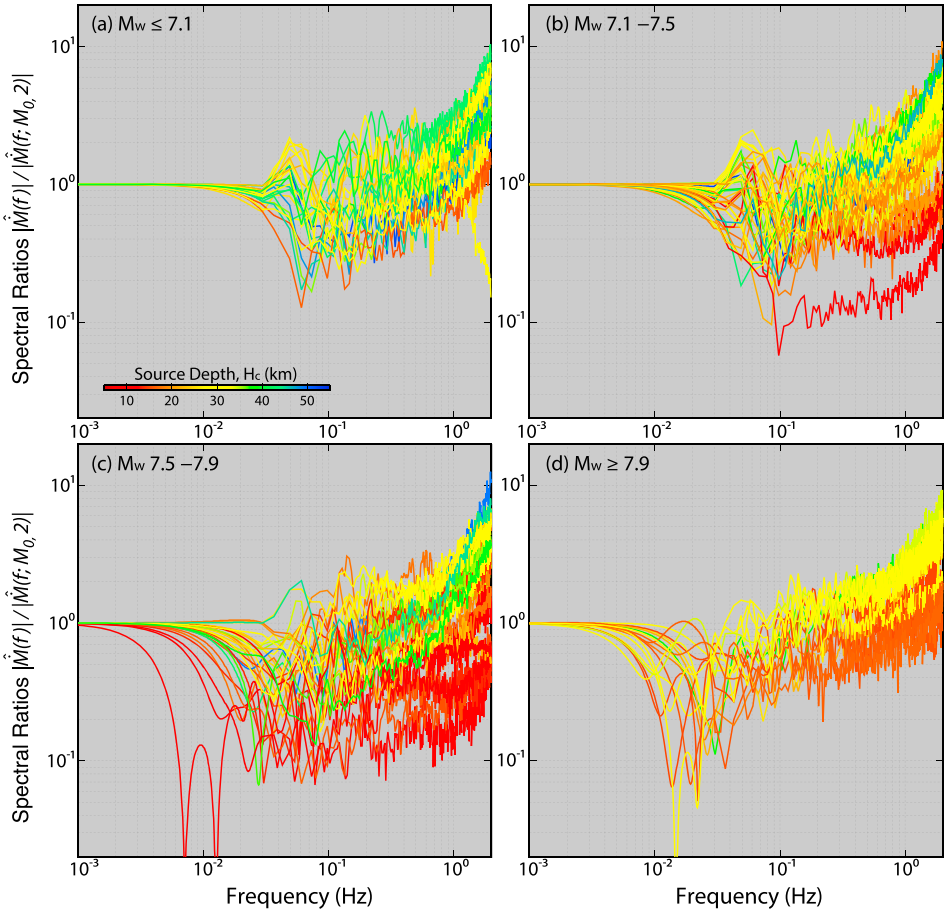

Figure 8. The ratios of observed spectra with respect to corresponding event ω^{-2} models, assuming a constant stress parameter of 3 MPa and $\beta = 3.75$ km/s, for events with (a) $M_w < 7.1$, (b) M_w 7.1–7.5, (c) M_w 7.5–7.9, and (d) $M_w > 7.9$. Colors indicate average depth of the slip distribution for each event.

Honshu earthquakes; these capture the basic features of the corresponding average source spectra (gray curves) other than the notching at intermediate periods which is a manifestation of the specific shape of the individual moment rate functions (we match only the amplitude spectra, not the phase spectra). We obtained $f_c = 12$ MHz, 35 MHz, and 35 MHz, and $n_0 = 1.59$, 1.63, and 1.42 for the three earthquakes with increasing source depths. Strong trade-off between the corner frequency and high-frequency decay rate is more evident for larger earthquakes, like the 1996 Peru, than for smaller earthquakes, like the 2014 Guerrero and 2005 Honshu, and this parameterization trade-off may blur the high-frequency characteristics from this model fitting presented below.

Our objective is not to precisely estimate the specific parameters of the spectral models and their formal uncertainties but rather to obtain stable overall characterizations of the spectra that permit comparisons between events. Figures 7 and 8 display the moment-normalized best-fitting ω^{-n_0} models and the ratios of each observed spectrum with respect to a reference ω^{-2} model, respectively, for all 114 events. The reference spectrum uses the seismic moment for each event and a Brune model stress parameter of 3 MPa with a shear velocity of 3.75 km/s and a scaling constant of 0.49. Because the corner frequency varies with magnitude, we compare the spectra for four magnitude bins (a) $M_w < 7.1$, (b) M_w 7.1–7.5, (c) M_w 7.5–7.9, and (d) $M_w \geq 7.9$. Figure 7 includes reference curves for spectral decay rates of ω^{-1} and ω^{-2}, and it is apparent that most events are fit by spectra with intermediate decay rates out to 1 Hz. Given that a consistent attenuation model is used for all events, we believe that the variability between events for different depths is a real feature, although both the absolute attenuation level and regional distribution of attenuation may vary between events. In both figures, there are systematic increases of the high-frequency radiation with source depth (the

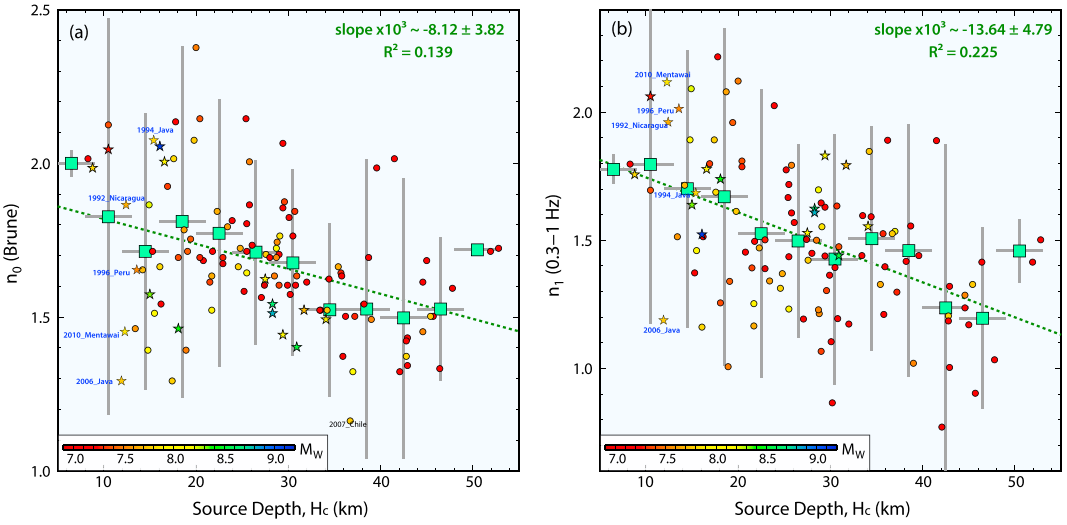

Figure 9. (a) High-frequency fall-off rate for the best-fitting ω^{-n_0} model for average event spectra and (b) regression slopes for the frequency band 0.3–1.0 Hz as functions of average depth of the slip distribution from the finite-fault source models. Colors of circles denote M_w. Colors of circles and stars denote M_w. The squares show the average value over each 5 km depth range as indicated by the horizontal gray lines. The vertical gray lines indicated the range of 2σ, where σ is the standard deviation. The coefficient of determination R^2 is shown for each case.

color coding) for magnitude ranges 7.1–7.5, 7.5–7.9, and 7.9–9.0 (Figures 7b–7d and 8b–8d) but large scatter for small events ($M_w < 7.1$) (Figures 7a and 8a). We explore this depth-varying behavior in the following sections 3.1–3.4.

3.1. High-Frequency Spectral Decay

Figure 9a shows the variation of high-frequency fall-off rate parameter, n_0, obtained from the spectral fitting (Figure 7) with the average source depth, H_c, from finite-fault inversions. The value of n_0 exhibits a large scatter for shallow events including the large tsunami earthquakes without obvious dependence on magnitude (indicated by symbol size). The average value of n_0 is about 1.64, and the mild depth dependence indicated by the regression curve suggests that deeper megathrust events may have slight enrichment in high-frequency spectral levels. The trend in the data that leads to the negative slope is clarified by plotting average values in 5 km depth bins (squares, with two standard deviation ranges indicated). The coefficient of determination, $R^2 = 0.139$.

Since there is some trade-off between n_0 and f_c in the spectral fitting and there is often notching of the source spectrum around the corner frequency, we use two additional simple parameters to more stably characterize the high-frequency spectral decay. We made simple linear regressions of the high-frequency source logarithmic spectrum to determine the slope (decay parameters) for frequency bands 0.3–1 Hz (n_1) and 0.3–2 Hz (n_2). These frequency bands are typically well beyond the corner frequency, as apparent in Figure 7. In most cases, we are confident about the source spectrum estimates up to ~1 Hz. For some events, the spectrum tends to flatten rapidly above 1 Hz as a result of hitting a noise floor, reducing n_2 compared to n_1, while in some cases mild concave upward curvature of the spectra is observed, also reducing n_2 compared to n_1. But in many cases the spectrum falls off smoothly out to 2 Hz with no indication of noise contamination (spectral slope fitting for all events is shown in Text S1). While still having large variability, these measures display quite clear trends of decreasing n_1 ($R^2 = 0.225$) (Figure 9b) and n_2 ($R^2 = 0.325$) (Figure S1a in the supporting information) with source depth, with stronger negative slopes, and less scatter than for n_0. The depth variation is more pronounced for n_2, but we consider those estimates somewhat less reliable overall.

The trend in Figure 9b, while capturing a limited bandwidth spectral behavior, further supports the interpretation that the relative level of high-frequency seismic radiation increases for deeper megathrust events [*Lay et al.*, 2012]. However, the net effect is somewhat obscured by the large variability. Although tsunami earthquakes are notable in having depleted high-frequency radiation, they are not distinct from other shallow earthquakes in their high-frequency decay rate (Figure 9b), indicating that the source radiation for all shallow

megathrust events is slightly different from that of deeper events. Consideration of the regional subduction zone patterns (Text S1) shows similar trends, albeit with lots of scatter, in several regions with sufficient data over a wide range of depths, including Central America, Peru/N. Chile, Vanuatu (New Hebrides), Solomon Islands, Sumatra, the Philippines, and Kuril/Kamchatka. This suggests that a widespread behavior underlies this modest depth dependence.

The various estimates of spectral decay slope (absolute values, n_0, n_1, and n_2) for $M_w \geq 7$ events are systematically smaller than 2 (Figure 9), whereas many smaller earthquakes appear to follow a standard ω^{-2} model [e.g., *Hough and Seeber*, 1991; *Shearer et al*., 2006]. Such low spectral decay rates are similar to observations by *Polet and Kanamori* [2000] and *Allmann and Shearer* [2009]. Since extrapolation of the lower decay rates to higher frequency would result in unbounded energy, the decay rate must increase at a higher frequency. The observed low decay rate may be a manifestation of "compound" ruptures of different scale asperities. As depth increases, a distribution of more small (high corner frequency) asperities and fewer large (low corner frequency) asperities could yield a composite spectrum that has a reduced slope over a limited frequency band. This scenario is consistent with the notion from *Lay et al*. [2012] that deeper events tend to be enriched in high-frequency radiation due to sampling a distinct population of small-scale asperities as the deep limit of the seismogenic zone is approached. Dynamic modeling of source spectra for models with multiscale heterogeneities would offer one way to test this idea further.

3.2. Radiated Energy

The total radiated seismic energy from a double-couple point source in a homogeneous whole space can be calculated from the source spectrum, $\hat{M}(f)$, by

$$E_R = \left[1 + \frac{3V_\alpha^5}{2V_\beta^5}\right] \cdot \frac{8\pi}{15\rho_h V_\alpha^5} \cdot \int_0^\infty f^2 \left|\hat{M}(f)\right|^2 \mathrm{d}f \tag{4}$$

or from the ground velocity spectrum, $\hat{u}(f)$, by

$$E_R = \left[1 + \frac{3V_\alpha^5}{2V_\beta^5}\right] \cdot \frac{128\pi^3 R_E^2}{15R(\theta,\varphi)^2} \cdot \frac{\rho_h V_\alpha}{g(\Delta)^2} \cdot \int_0^\infty \hat{u}(f)^2 \mathrm{d}f, \tag{4a}$$

where notations are the same as for equation (2). Based on equation (4a), we determine the radiated energy for each station from the observed ground velocity spectra following the method of *Venkataraman and Kanamori* [2004] and then average the station estimates in a logarithmic sense to estimate the radiated energy for frequencies above 0.05 Hz. The time window for each event is carefully chosen to include most *P* wave group arrivals while minimizing the scattered coda energy and *PP* phases. For some events there is a substantial fraction of radiated seismic energy at frequencies less than 0.05 Hz, especially for tsunami earthquakes [*Ye et al*., 2013b; *Lay et al*., 2013a]. We account for the low-frequency radiated energy as follows. First, from each source spectrum as shown in Figure 6, we estimate the ratio of cumulative energy over the low-frequency band, $f \leq 0.05$ Hz, to the high-frequency band, $f \geq 0.05$ Hz. This does not involve the absolute energy. Then we scale the average radiated energy estimates for $f \geq 0.05$ Hz using (4a) with this ratio to retrieve the low-frequency contribution and total radiated energy.

Uncertainties in radiated energy estimates are introduced by lack of constraint on the average *P* and *S* wave velocities around the source, limited data bandwidth, uncertainty in wave propagation corrections (particularly attenuation), uncertainties in radiation pattern corrections, and source directivity effects. It is also recognized that the free surface interaction for very shallow events may lead to overestimation of the low-frequency energy [*Rivera and Kanamori*, 2014]. *Venkataraman and Kanamori* [2004] show that the directivity corrections for dip-slip earthquakes with rupture that expands primarily along strike are generally less than a factor of 2, and we tried to include data with as uniform azimuthal coverage as possible to reduce this effect.

Figure 10a shows our radiated energy estimates for the 114 $M_w \geq 7$ events in this study computed for an upper frequency limit of 1 Hz. For three events larger than M_w 8.5, we adopt E_R estimates reported by *Lay et al*. [2012] (Table S1 in Paper 1) because special efforts were made to determine the long-period energy contributions that dominate the radiated energy for those huge events. It is hard to define a uniform upper limit of frequency given the low S/N ratio in teleseismic *P* wave recordings for events of variable size, but 1 Hz

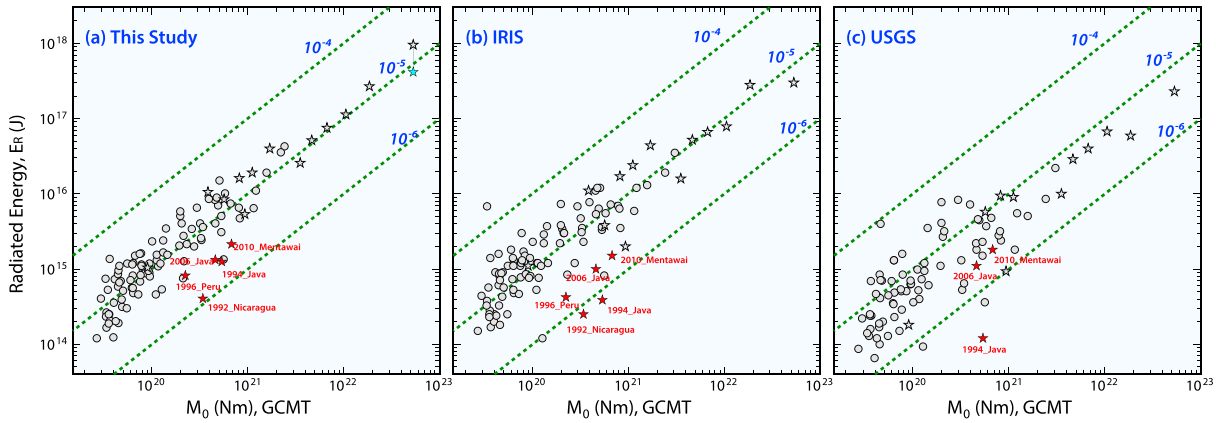

Figure 10. Estimates of radiated energy for the events considered in this study from (a) this analysis, using the procedure described in the text (circles for models with assumed V_r and stars for models with independent estimates of V_r). Most results for this study for giant earthquakes ($M_w > 8.5$) are comparable with those from *Lay et al.* [2012], except large discrepancy for the 2011 M_w 9.1 Tohoku earthquake as indicated by the cyan star. (b) IRIS implementation of the method of *Convers and Newman* [2011] and (c) USGS-NEIC [*Boatwright and Choy*, 1986], as functions of GCMT seismic moment. The measures for large tsunami earthquakes are labeled in red. The dashed curves are for constant logarithmic scaling of E_R versus M_0.

appears to be compatible with most of the observed source spectral noise levels. The absolute levels of the high-frequency energy estimates depend on the attenuation model, which is approximated as being uniform but certainly has path-dependent variations that are averaged in each case. Many spectra appear to be well behaved up to about 2 Hz (or higher), but some are contaminated by noise. If we uniformly compute radiated energy estimates using frequencies up to 2 Hz, higher radiated energy estimates are, of course, obtained. There are substantial differences, up to about a factor of 2, in radiated energy estimates for smaller events ($M_w \sim 7.0$–7.4) when using upper frequency limits of 1 Hz versus 2 Hz and modest differences for large events ($M_w > \sim 7.5$) but no obvious bias for events at different source depths. If we compare our up-to-1 Hz estimates of radiated energy with routine catalog estimates for the same events, we find good consistency with broadband estimates from the Incorporated Research Institutions for Seismology SPUD implementation of the method of *Convers and Newman* [2011] (http://www.iris.edu/spud/eqenergy) (Figure 10b) but somewhat higher values than the U.S. Geological Survey National Earthquake Information Center (USGS-NEIC) estimates based on *Boatwright and Choy* [1986] (Figure 10c). The latter difference may be due to our inclusion of the additional contribution from low frequencies, differences in frequency bandwidth used, differences in assumed contribution from S wave energy, or differences in the attenuation models used. The large tsunami earthquakes stand out as having low radiated energy for all three databases. The depth-dependent distribution of radiated energy will be quantified in detail below.

3.3. Moment-Scaled Radiated Energy and Apparent Stress

The radiated energy E_R scaled by seismic moment M_0 is an important measure of the rupture processes and has been explored for investigation of depth-varying characteristics [e.g., *Lay et al.*, 2012; *Ma and Hirakawa*, 2013]. Figure 11a shows our measurements of this ratio using the radiated energy estimates up to 1 Hz as functions of source depth H_c. The highlighted tsunami earthquakes clearly stand out from the other large megathrust events in this study, along with other earthquakes with strong observed tsunami or very shallow ruptures such as the 17 November 2000 (21:01 GMT) Papua event [*Geist and Parsons*, 2005], 27 August 2012 El Salvador earthquake [*Ye et al.*, 2013b], and 6 February 2013 Santa Cruz Island earthquake [*Lay et al.*, 2013a]. Relatively low values for the 1990 Costa Rica and the deeper Papua events are of interest for further examination. The low E_R/M_0 of the tsunami events relative to other comparably large earthquakes is compatible with the results of *Newman and Okal* [1998]. Moment-scaled radiated energy measures have large scatter from 1×10^{-6} to 4×10^{-5} with an average of $\sim1.06\times10^{-5}$ but no apparent magnitude (Paper 1) or depth dependence apart from the shallow tsunami event population. There is a subtle increasing trend with source depth in some individual subduction zones such as Mexico, Central America, Vanuatu (New Hebrides), and Japan (see Text S1), but the data are too sparse to place much confidence in those trends at this time.

Apparent stress, defined as the product of the rigidity and moment-scaled radiated energy, has often been related to dynamic rupture processes (Paper 1). If rigidity is assumed to be constant for all megathrust

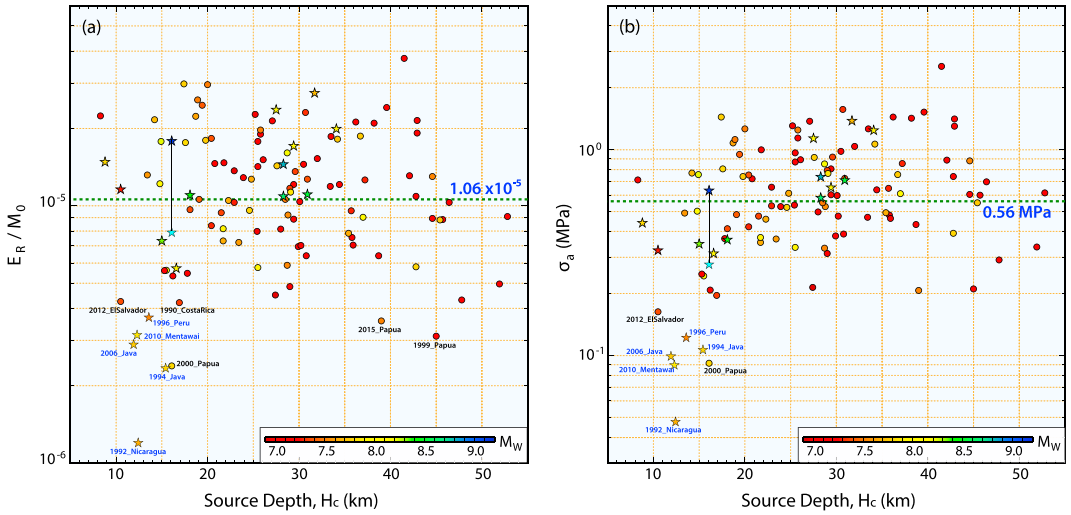

Figure 11. (a) Moment-scaled radiated energy and (b) apparent stress, plotted as functions of average depth of the slip distribution for the finite-fault models. The cyan star indicates the moment-scaled radiated energy and apparent stress for the 2011 M_W 9.1 Tohoku earthquake calculated with the radiated energy from *Lay et al.* [2012]. Tsunami earthquakes are highlighted by blue labels. The symbol colors denote M_W.

environments, say 30 GPa, as used in many previous studies, the apparent stress would be directly proportional to moment-scaled radiated energy presented in Figure 11a. We compute apparent stress using the depth-dependent rigidity determined from the velocity models incorporated in our finite-fault inversions. The slip-weighted average rigidity for the rupture model is used as the effective rigidity. Resulting variations of apparent stress with the source depth for our major and large events (Figure 11b) are naturally quite similar to the moment-scaled radiated energy patterns, but the shallow tsunami earthquakes are more distinctive, due to the product of low E_R/M_0 and low source region rigidity. The average value is 0.56 MPa. The overall pattern of apparent stress, with an increasing trend at shallow depth ($H_c < \sim 18$ km) but no trend at larger depth, is similar to that in moment-scaled source duration and $V_r^3 \Delta\sigma_E$. Because the actual values of rigidity, particularly at very shallow depth, in the megathrust environment are not well constrained, it is hard to formally estimate uncertainties in the apparent stress values. However, apart from the baseline shift to low values around 0.1 MPa for the tsunami earthquakes and some other shallow events, there is no clear dependence on earthquake depth over the megathrust for our global population of major and great events at large source depths. The individual subduction zones with a pattern of increasing moment-scaled radiated energy with increasing depth noted above all have slightly more pronounced patterns for apparent stress due to the increase in rigidity with depth in our source models (Text S1).

3.4. High-Frequency Radiated Energy Fraction

A systematic way to detect any depth variation in the relative amount of high-frequency radiated energy above a frequency, f_1, is to compute the ratio, $r(f_1)$, of high-frequency radiated energy to the total radiated energy. For an ω^{-2} model this ratio is given by

$$\begin{aligned} r(f_1) &= \frac{E_R(f_1 \to \infty)}{E_R(0 \to \infty)} \\ &= \frac{4f_c}{\pi}\int_0^\infty \frac{f^2}{\left(f^2 + f_c^2\right)^2} \mathrm{d}f \\ &= 1 - \frac{2}{\pi}\left[\tan^{-1}\left(\frac{f_1}{f_c}\right) - \frac{f_1 \cdot f_c}{f_1^2 + f_c^2}\right]. \end{aligned} \tag{5}$$

As $f_1 >> f_c$, the ratio approaches

$$r(f_1) \to \frac{2}{\pi}\frac{f_c}{f_1}. \tag{6}$$

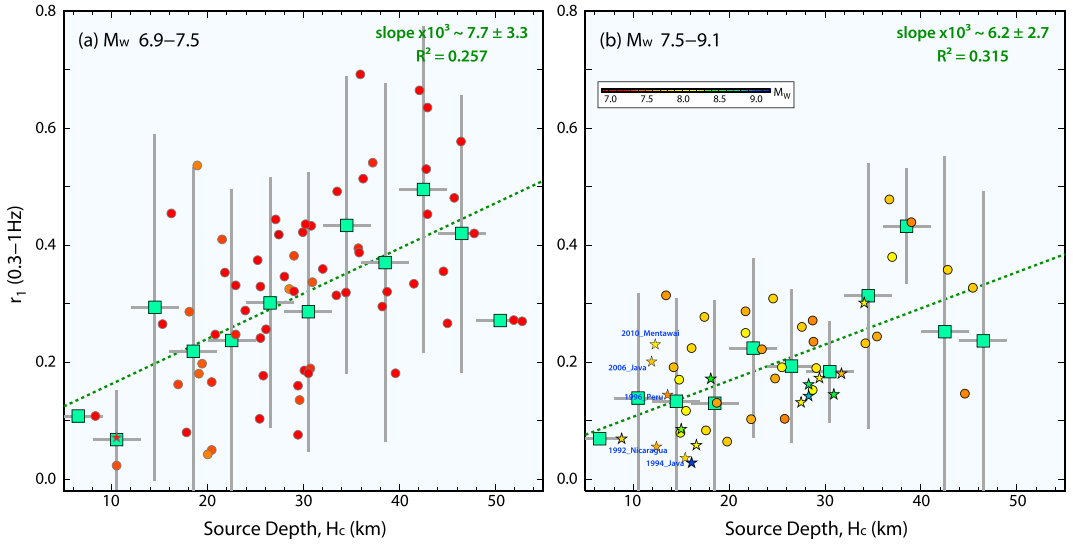

Figure 12. Ratios of high-frequency (0.3–1.0 Hz) radiated energy over total radiated energy for events with (a) M_w 6.9–7.5 and (b) M_w 7.5–9.1, plotted as functions of average depth of the slip distribution for the finite-fault models. Tsunami earthquakes are highlighted by blue labels. The symbol colors denote M_w. The squares show the average value over each 5 km depth range as indicated by the horizontal gray lines. The vertical gray lines indicated the range of 2σ, where σ is the standard deviation. The coefficient of determination R^2 is shown for each case.

This shows that the high-frequency radiated energy ratio is essentially controlled by the corner frequency. Since $f_c \propto M_0^{-1/3}$, this ratio is magnitude-dependent for a uniform f_1. To assess any variation of high-frequency energy with centroid depth, we show the high-frequency ratios for two magnitude bins in Figure 12. There is certainly a scatter but a clear positive slope of the ratio (high-frequency energy from 0.3 to 1 Hz)/(total radiated energy) with source depth for events with M_w 6.9–7.5 ($R^2 = 0.257$) and M_w 7.5–9.1 ($R^2 = 0.315$). Even stronger trends are found for energy ratios using the radiated energy computed from 0.3 to 2.0 Hz ($R^2 = 0.424$) (Figure S1b). This behavior is consistent with what was found for the high-frequency decay rate of the source spectrum, as it is essentially an integral measure of the same spectral behavior. Among the individual subduction zones,

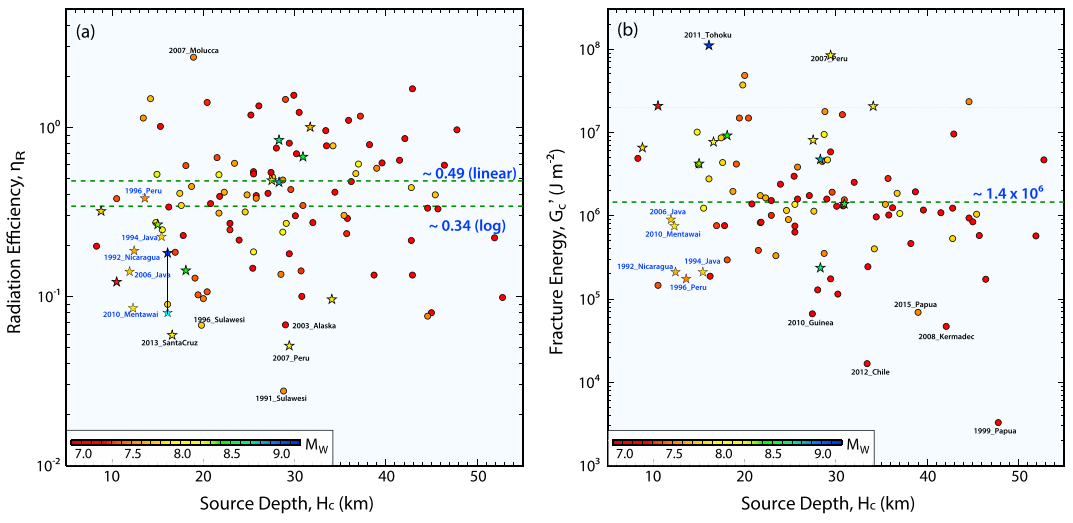

Figure 13. (a) Radiation efficiency and (b) fracture energy G' (for those cases with radiation efficiency less than 1.0), plotted as functions of average depth of the slip distribution for the finite-fault models. The cyan star indicates the radiation efficiency and fracture energy for the 2011 M_w 9.1 Tohoku earthquake calculated with the radiated energy from *Lay et al.* [2012]. Events with high or low values are labeled. The linear and log averages of the entire population are indicated by the labeled green dashed lines. Tsunami earthquakes are highlighted by blue. The symbol colors denote M_w.

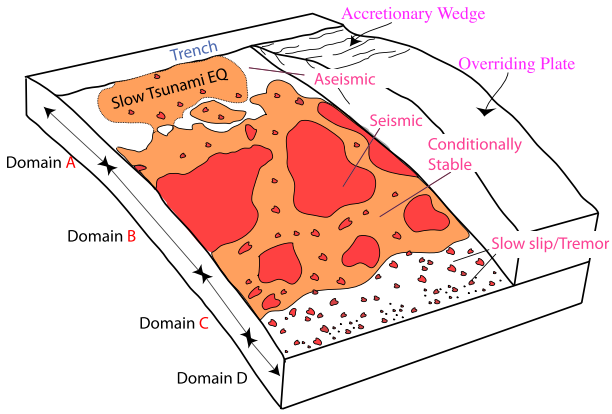

Figure 14. Cutaway schematic characterization of the megathrust frictional environment, related to domains A, B, and C defined in Figure 1. Regions of unstable frictional sliding are red regions labeled "seismic." Regions of aseismic stable or episodic sliding are white regions labeled "aseismic." Orange areas are conditional stability [*Scholz*, 1998] regions, which displace aseismically except when accelerated by failure of adjacent seismic patches. Domain A is at shallow depth where sediments and pore fluids cause very slow rupture expansion even if large displacements occur in tsunami earthquakes. Domain B has large, relatively uniform regions of stable sliding that can have large slip but generate modest amounts of high-frequency radiation upon failure. Domain C has patchy, smaller-scale regions of stable sliding surrounded by conditionally stable areas. When these areas fail, coherent high-frequency radiation is produced. Small, isolated patches may behave as repeaters when quasi-static sliding of surrounding regions regularly load them to failure. Domain D is dominated by aseismic sliding, but many small unstable patches can rupture in seismic tremor when slow slip events occur. Modified from *Lay* [2015].

a corresponding pattern is observed for Peru/N. Chile, New Zealand, Vanuatu (New Hebrides), Sumatra, and Kuril/Kamchatka (Text S1). The increase in relative amount of high-frequency radiated energy is systematic but too weak to cause the total moment-scaled radiated energy to display a strong trend with source depth. The increase in $r(f_1)$ with depth is important for understanding strong ground-shaking hazard produced by the high-frequency part of the spectrum.

4. Discussion

Determining physical controls on seismic rupture characteristics of plate boundary megathrust faults is challenging due to observational limitations of both the seismic and environmental parameters, as well as the existence of both along-strike and along-dip variations. Distinctive tsunami earthquake rupture properties, such as unusually long source duration, low rupture velocities, low static stress drop, low moment-scaled radiated energy, and large slip to the trench, have been related to low source region rigidity associated with subducted sediments [*Kanamori and Kikuchi*, 1993]. Additionally, tsunami earthquake characteristics have been related to rupture on splay faults or backstop frontal faults in addition to the main megathrust [*Moore et al.*, 2007]. Anelastic deformation of the sedimentary wedge during shallow ruptures has also been proposed to explain properties of tsunami earthquakes [*Ma and Hirakawa*, 2013]. Several physical parameters, such as fluid distribution and pore pressures, mineralogical composition related with dehydration processes, incoming plate morphological structure, and rate- and state-dependent frictional conditions, have been invoked to explain variable high-frequency seismic radiation for deep events along megathrusts [e.g., *Lay and Bilek*, 2007].

4.1. Frictional Heterogeneity on the Megathrust

The lack of depth dependence of static stress drop ($\Delta\sigma_E$) for major and great megathrust earthquakes globally and in individual subduction zones indicates that the observed seismic radiation characteristics are largely insensitive to normal stress variations. In addition, we find no clear trends with source depth for the dynamic source parameters discussed in Paper 1, radiation efficiency η_R and fracture energy per unit area G (Figure 13). The radiation efficiency is defined as the ratio of radiated energy to the total available potential energy (ΔW_0), i.e., $\eta_R = \frac{E_R}{\Delta W_0} = \frac{2\mu}{\Delta\sigma} \cdot \frac{E_R}{M_0} = 2 \cdot \frac{\sigma_a}{\Delta\sigma}$ which involves the ratio of the apparent stress to static stress drop. The absence of depth dependence of radiation efficiency implies that there is no systematic variation of energy partitioning during earthquake rupture with source depth. These observations suggest that overall dynamic rupture processes are relatively insensitive to source depth, and the systematic, although modest enrichment of high-frequency seismic radiation with increasing source depth may be the results of heterogeneity on the rupture surface along the megathrust.

The notion of depth-dependent scale lengths of megathrust heterogeneities (Figure 14) has been advanced as a means for explaining the depth variation of seismic radiation illustrated by the schematic model in Figure 1 [*Lay et al.*, 2012]. Large aseismic or conditionally stable regions at shallow depth (domain A with source depth $< \sim 18$ km) arising from the presence of sediments and pore fluids may produce slow rupture

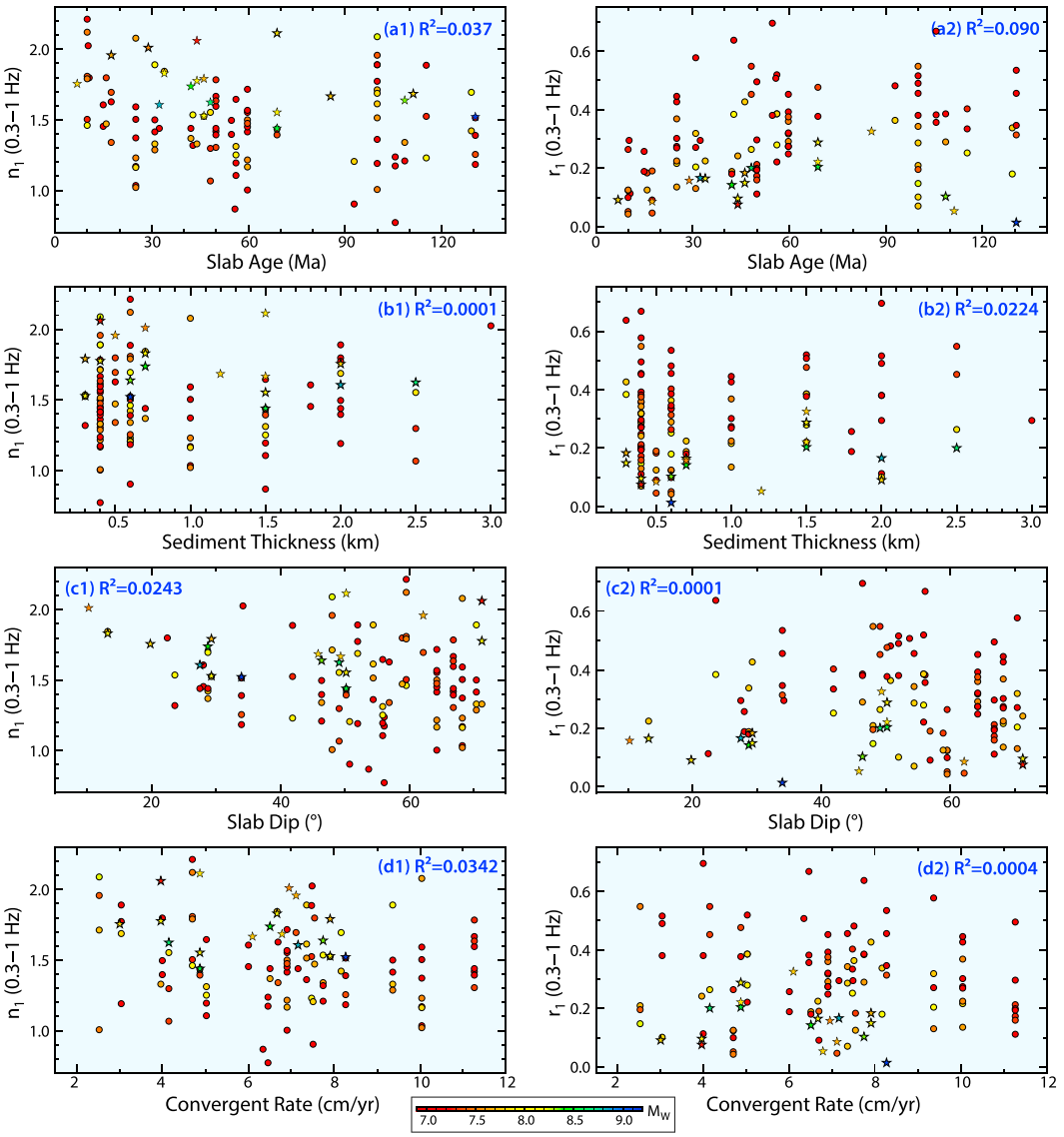

Figure 15. High-frequency regression slopes for the 0.3–1.0 Hz spectral range (left) and ratios of high-frequency (0.3–1 Hz) radiated energy over the total radiated energy (right), versus (a) subducted slab ages, (b) sediment thickness, (c) slab dip angles, and (d) convergent velocities [*Syracuse et al.*, 2010]. The symbol colors denote M_w. The coefficient of determination R^2 is shown for each case.

expansion and inefficient seismic wave generation, resulting in low moment-scaled radiated energy and significantly low apparent stress enhanced by low rigidity, even though large displacements occur in tsunami earthquakes. At source depths spanning from 15 to 30 km, there are large, relatively uniform regions with unstable sliding frictional properties, i.e., asperities, or area with large coseismic slip, that generate modest amounts of spatially distributed high-frequency radiation upon failure. The downdip part of the megathrust may be enriched in patchy, smaller-scale asperities surrounded by "aseismic" conditionally stable areas, which would produce enhanced localized bursts of high-frequency seismic radiation during rupture. In general, the depth-varying properties of sediments at shallow depths from 5 to ~18 km may contribute to a step change or rapidly increasing trend of moment-scaled duration and apparent stress. The increase of high-frequency radiated energy fraction, and the associated decrease of high-frequency decay rate, with source depth may be related with gradual increase of the percentage of isolated, small-scale asperities as shown in Figure 14. Further quantitative modeling of effects on seismic radiation from sediments and multiple-scale heterogeneities along the megathrust, such as that done by *Noda and Lapusta* [2013], framed by the extensive kinematic observations presented in this study, is desirable.

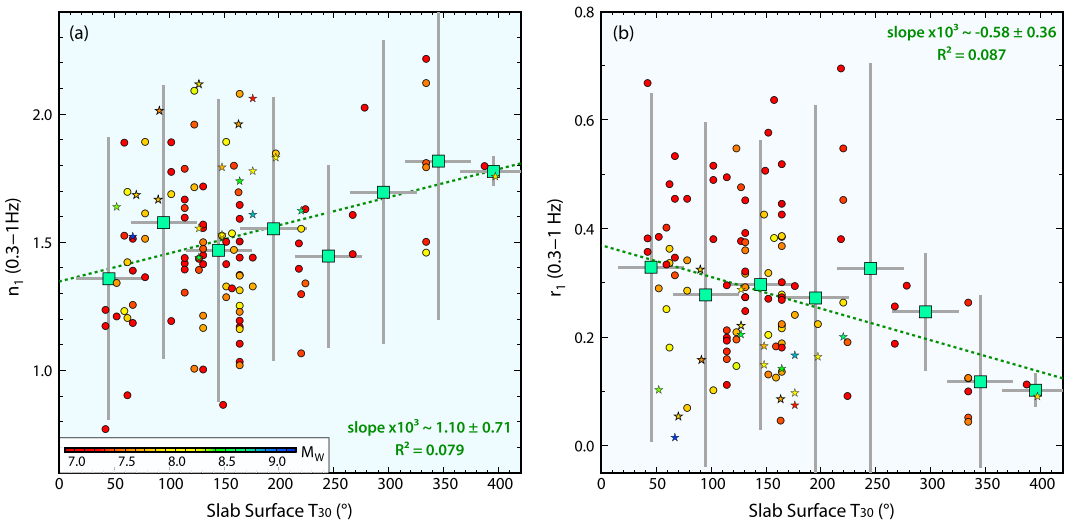

Figure 16. (a) High-frequency regression slopes for the 0.3–1 Hz spectral range and (b) ratios of high-frequency (0.3–1 Hz) radiated energy over the total radiated energy, versus estimates of surface temperature of the subducting slab at 30 km depth [*Syracuse et al*., 2010]. Colors of circles and stars denote M_W. The squares show the average value over each 50° range as indicated by the horizontal gray lines. The vertical gray lines indicated the range of 2σ, where σ is the standard deviation. The coefficient of determination R^2 is shown for each case.

4.2. Correlation With Slab Properties

The global sampling provided by the data set in this study enables some tests of correlation of seismic radiation attributes with pressure- and/or temperature-dependent properties of the megathrust. We correlate the depth-varying high-frequency spectral decay and high-frequency radiated energy ratio estimates from this study with estimates of slab age, slab dip angle, plate convergence velocity, and sediment thickness as summarized by *Syracuse et al*. [2010], along with 2-D kinematically modeled slab surface temperature at 30 km depth for 56 segments of global subduction zones [*Syracuse et al*., 2010]. We did not find systematic trends for both high-frequency seismic radiation measures as a function of slab age, geometry, convergent rate, or sediment thickness (Figure 15).

However, we find some (admittedly weak) correlation between both high-frequency spectral slopes and high-frequency radiated energy ratios with slab temperature at 30 km (Figures 16 and S2), with the sense that relatively enriched high-frequency seismic radiation correlates with colder slab interface conditions. As there could be a systematic reduction of average attenuation factor with increasing depth or decreasing slab interface temperature, we cannot uniquely attribute this tendency to temperature effects on frictional properties or on stress heterogeneity, but further work to explore any temperature relationships to seismic radiation is encouraged. The sense of correlation that we find for the global data set is consistent with the regional results found for the Japan trench megathrust, where the extensive high-quality regional seismic data allowed inference that observed strong high-frequency ground shaking from deep megathrust events is due to a combination of relatively enriched high-frequency source spectra and low attenuation path effects [*Ye et al*., 2013a].

5. Conclusions

Depth-dependent variations of rupture characteristics for 114 $M_w \geq 7$ interplate subduction zone megathrust earthquakes from 1990 to 2015 have been explored. The source characteristics are estimated using uniform methodologies, finite-fault inversion, and source spectrum analysis applied to teleseismic body wave observations. There is no trend of moment-scaled source duration and centroid time, static stress drop, or moment-scaled radiated energy with depth other than low values being found for very shallow tsunami earthquakes and a few other shallow events. However, there is a moderate systematic increase in the relative amount of high-frequency seismic radiation for deeper megathrust events, manifested in reduced high-frequency fall-off slopes of the average source spectra and increased ratios of high-frequency radiated

energy to total radiated energy as depth increases. There is a weak correlation of these high-frequency measures with estimated average megathrust temperature, with colder megathrust environments tending to have somewhat enriched high-frequency radiation. This raises the possibility that the depth-varying seismic characteristics may result from frictional and/or attenuation variations influenced by temperature. Statistical comparisons of seismic measurements with slab and plate interface parameters require larger data sets to consider two-dimensional and regional variations. Efforts to directly estimate physical variations of large ruptures, such as size and patterns of large slip patches on megathrusts, could potentially help to reveal the mechanisms of the observed depth-varying rupture characteristics.

Acknowledgments
This work made use of GMT and SAC software. We appreciate comments from the Associate Editor, Gavin Hayes, and an anonymous reviewer. Rachel Abercrombie and an anonymous reviewer provided helpful reviews of an earlier version of the manuscript. The Incorporated Research Institutions for Seismology data management center was used to access the seismic data from Global Seismic Network and Federation of Digital Seismic Network stations. This work was supported by U.S. National Science Foundation grant EAR1245717 (T.L.). Digital information about the moment rate functions and finite-fault slip models for all events can be found at https://sites.google.com/site/linglingye001/earthquakes/slip-models.

References

Allmann, B. P., and P. M. Shearer (2009), Global variations of stress drop for moderate to large earthquakes, *J. Geophys. Res.*, *114*, B01310, doi:10.1029/2008JB005821.

Bilek, S. L., H. R. DeShon, and E. R. Engdahl (2012), Spatial variations in earthquake source characteristics within the 2011 M_w = 9.0 Tohoku, Japan rupture zone, *Geophys. Res. Lett.*, *39*, L09304, doi:10.1029/2012GL051399.

Boatwright, J., and G. L. Choy (1986), Teleseismic estimates of the energy radiated by shallow earthquakes, *J. Geophys. Res.*, *91*, 2095–2112, doi:10.1029/JB091iB02p02095.

Brune, J. (1970), Tectonic stress and the spectra of seismic shear waves from earthquakes, *J. Geophys. Res.*, *75*, 4997–5009.

Choy, G. L., A. McGarr, S. H. Kirby, and J. Boatwright (2006), An overview of the global variability in radiated energy and apparent stress, in *Earthquakes: Radiated Energy and the Physics of Faulting*, *Geophys. Monogr. Ser.*, vol. 170, pp. 43–57, AGU, Washington, D. C., doi:10.1029/170GM06.

Convers, J. A., and A. V. Newman (2011), Global evaluation of large earthquake energy from 1997 through mid-2010, *J. Geophys. Res.*, *116*, B08304, doi:10.1029/2010JB007928.

Duputel, Z., V. C. Tsai, L. Rivera, and H. Kanamori (2013), Using centroid time-delays to characterize source durations and identify earthquakes with unique characteristics, *Earth Planet. Sci. Lett.*, *375*, 92–100, doi:10.1016/j.epsl.2013.05.024.

Ekström, G., M. Nettles, and A. M. Dziewonski (2012), The global CMT project 2004–2010: Centroid-moment tensors for 13,017 earthquakes, *Phys. Earth Planet. Inter.*, *200–201*, 1–9, doi:10.1016/j.pepi.2012.04.002.

El Hariri, M., S. L. Bilek, H. R. DeShon, E. R. Engdahl, and S. Bisrat (2013), Along-strike variability of rupture duration in subduction zone earthquakes, *J. Geophys. Res. Solid Earth*, *118*, 646–664, doi:10.1029/2012JB009548.

Geirsson, H., P. C. LaFemina, C. DeMets, D. A. Hernandez, G. S. Mattioli, R. Rogers, M. Rodriguez, G. Marroquin, and V. Tenorio (2015), The 2012 August 27 M_W7.3 El Salvador earthquake: Expression of weak coupling on the Middle America subduction zone, *Geophys. J. Int.*, *202*(3), 1677–1689.

Geist, E. L., and T. Parsons (2005), Triggering of tsunamigenic aftershocks from large strike-slip earthquakes: Analysis of the November 2000 New Ireland earthquake sequence, *Geochem. Geophys. Geosyst.*, *6*, Q10005, doi:10.1029/2005GC000935.

Hough, S., and L. Seeber (1991), Seismological constraints on source properties of the m_b = 4.0 Ardsley, New York earthquake: A characteristic rupture?, *J. Geophys. Res.*, *96*, 18,183–18,195.

Kanamori, H. (2014), The diversity of large earthquakes and its implications for hazard mitigation, *Annu. Rev. Earth Planet. Sci.*, *42*, 7–26, doi:10.1146/annurev-earth-060313-055034.

Kanamori, H., and M. Kikuchi (1993), The 1992 Nicaragua earthquake: A slow tsunami earthquake associated with subducted sediments, *Nature*, *361*, 714–716.

Lay, T. (2015), The surge of great earthquakes from 2004 to 2014, *Earth Planet. Sci. Lett.*, *409*, 133–146.

Lay, T., and S. L. Bilek (2007), Anomalous earthquake ruptures at shallow depths on subduction zone megathrusts, in *The Seismogenic Zone of Subduction Thrust Faults*, edited by T. Dixon and C. Moore, pp. 476–511, Columbia Univ. Press, New York.

Lay, T., C. J. Ammon, A. R. Hutko, and H. Kanamori (2010), Effects of kinematic constraints on teleseismic finite-source rupture inversions: Great Peruvian earthquakes of 23 June 2001 and 15 August 2007, *Bull. Seismol. Soc. Am.*, *100*, 969–994, doi:10.1785/0120090274.

Lay, T., H. Kanamori, C. J. Ammon, K. D. Koper, A. R. Hutko, L. Ye, H. Yue, and T. Rushing (2012), Depth-varying rupture properties of subduction zone megathrust faults, *J. Geophys. Res.*, *117*, B04311, doi:10.1029/2011JB009133.

Lay, T., L. Ye, H. Kanamori, Y. Yamazaki, K. F. Cheung, and C. J. Ammon (2013a), The February 6, 2013 M_w 8.0 Santa Cruz Islands earthquake and tsunami, *Tectonophysics*, *608*, 1109–1121, doi:10.1016/j.tecto.2013.07.001.

Lay, T., L. Ye, H. Kanamori, Y. Yamazaki, K. F. Cheung, K. D. Koper, and K. Kwong (2013b), The October 28, 2012 M_w 7.8 Haida Gwaii underthrusting earthquake and tsunami: Slip partitioning along the Queen Charlotte Fault transpressional plate boundary, *Earth Planet. Sci. Lett.*, *375*, 57–70, doi:10.1016/j.epsl.2013.05.005.

Ma, S., and E. T. Hirakawa (2013), Dynamic wedge failure reveals anomalous energy radiation of shallow subduction earthquakes, *Earth Planet. Sci. Lett.*, *375*, 113–122.

Moore, G. F., N. L. Bangs, A. Taira, S. Kuramoto, E. Pangborn, and H. J. Tobin (2007), Three-dimensional splay fault geometry and implications for tsunami generation, *Science*, *318*, 1128–1131, doi:10.1126/science.1147195.

Newman, A. V., and E. A. Okal (1998), Teleseismic estimates of radiated seismic energy: The E/M_0 discriminant for tsunami earthquakes, *J. Geophys. Res.*, *103*, 26,885–26,898, doi:10.1029/98JB02236.

Noda, H., and N. Lapusta (2013), Stable creeping fault segments can become destructive as a result of dynamic weakening, *Nature*, *493*(7433), 518–521.

Noda, H., N. Lapusta, and H. Kanamori (2013), Comparison of average stress drop measures for ruptures with heterogeneous stress change and implications for earthquake physics, *Geophys. J. Int.*, *193*(3), 1691–1712, doi:10.1093/gji/ggt074.

Pérez-Campos, X., S. K. Singh, and G. C. Beroza (2003), Reconciling teleseismic and regional estimates of seismic energy, *Bull. Seismol. Soc. Am.*, *93*(5), 2123–2130.

Polet, J., and H. Kanamori (2000), Shallow subduction zone earthquakes and their tsunamigenic potential, *Geophys. J. Int.*, *142*, 684–702, doi:10.1046/j.1365-246x.2000.00205.x.

Polet, J., and H. Kanamori (2009), Tsunami earthquakes, in *Encyclopedia of Complexity and Systems Science*, pp. 9577–9592, Springer, New York.

Rivera, L., and H. Kanamori (2014), Estimation of radiated energy of recent great earthquakes using the normal-mode theory, AGU Fall Meeting 2014 Abstract S53B-4502.

Scholz, C. (1998), Earthquakes and friction laws, *Nature*, *391*, 37–42.

Shearer, P. M., G. A. Prieto, and E. Hauksson (2006), Comprehensive analysis of earthquake source spectra in southern California, *J. Geophys. Res.*, *111*, B06303, doi:10.1029/2005JB003979.

Syracuse, E. M., P. E. van Keken, and G. A. Abers (2010), The global range of subduction zone thermal models, *Phys. Earth Planet. Inter.*, *183*(1), 73–90.

Venkataraman, A., and H. Kanamori (2004), Observational constraints on the fracture energy of subduction zone earthquakes, *J. Geophys. Res.*, *109*, B05302, doi:10.1029/2003JB002549.

Ye, L., T. Lay, and H. Kanamori (2012a), The Sanriku-Oki low-seismicity region on the northern margin of the great 2011 Tohoku-Oki earthquake rupture, *J. Geophys. Res.*, *117*, B02305, doi:10.1029/2011JB008847.

Ye, L., T. Lay, and H. Kanamori (2012b), Intraplate and interplate faulting interactions during the August 31, 2012, Philippine Trench earthquake (M_w 7.6) sequence, *Geophys. Res. Lett.*, *39*, L24310, doi:10.1029/2012GL054164.

Ye, L., T. Lay, and H. Kanamori (2013a), Ground shaking and seismic source spectra for large earthquakes around the megathrust fault offshore of northeastern Honshu, Japan, *Bull. Seismol. Soc. Am.*, *103*(2B), 1221–1241, doi:10.1785/0120120115.

Ye, L., T. Lay, and H. Kanamori (2013b), Large earthquake rupture process variations on the Middle America megathrust, *Earth Planet. Sci. Lett.*, *381*, 147–155, doi:10.1016/j.epsl.2013.08.042.

Ye, L., T. Lay, H. Kanamori, and K. D. Koper (2013c), Energy release of the 2013 M_w 8.3 Sea of Okhotsk earthquake and deep slab stress heterogeneity, *Science*, *341*, 1380–1384, doi:10.1126/science.1242032.

Ye, L., T. Lay, H. Kanamori, and L. Rivera (2016), Rupture characteristics of major and great ($M_w \geq 7.0$) megathrust earthquakes from 1990 to 2015. 1. Source parameter scaling relationships, *J. Geophys. Res. Solid Earth*, *121*, doi:10.1002/2015JB012426.

Journal of Geophysical Research

Supporting Information for

Rupture Characteristics of Major and Great ($M_w \geq 7.0$) Megathrust Earthquakes from 1990-2015: II. Depth-Dependence

Lingling Ye[1,2], Thorne Lay[1], Hiroo Kanamori[2], Luis Rivera[3]

1. Department of Earth and Planetary Sciences, University of California Santa Cruz, Santa Cruz, CA 95064, USA.
2. Seismological Laboratory, California Institute of Technology, Pasadena, CA 91125 USA.
3. Institut de Physique du Globe de Strasbourg (UMR7516), Université de Strasbourg/CNRS, Strasbourg, France.

Contents of this file

Additional Supporting Information (Files uploaded separately)

Supplement S1 – Figures S3 to S36: Finite-fault models for 17 subregions with source parameter relations for all events in each region

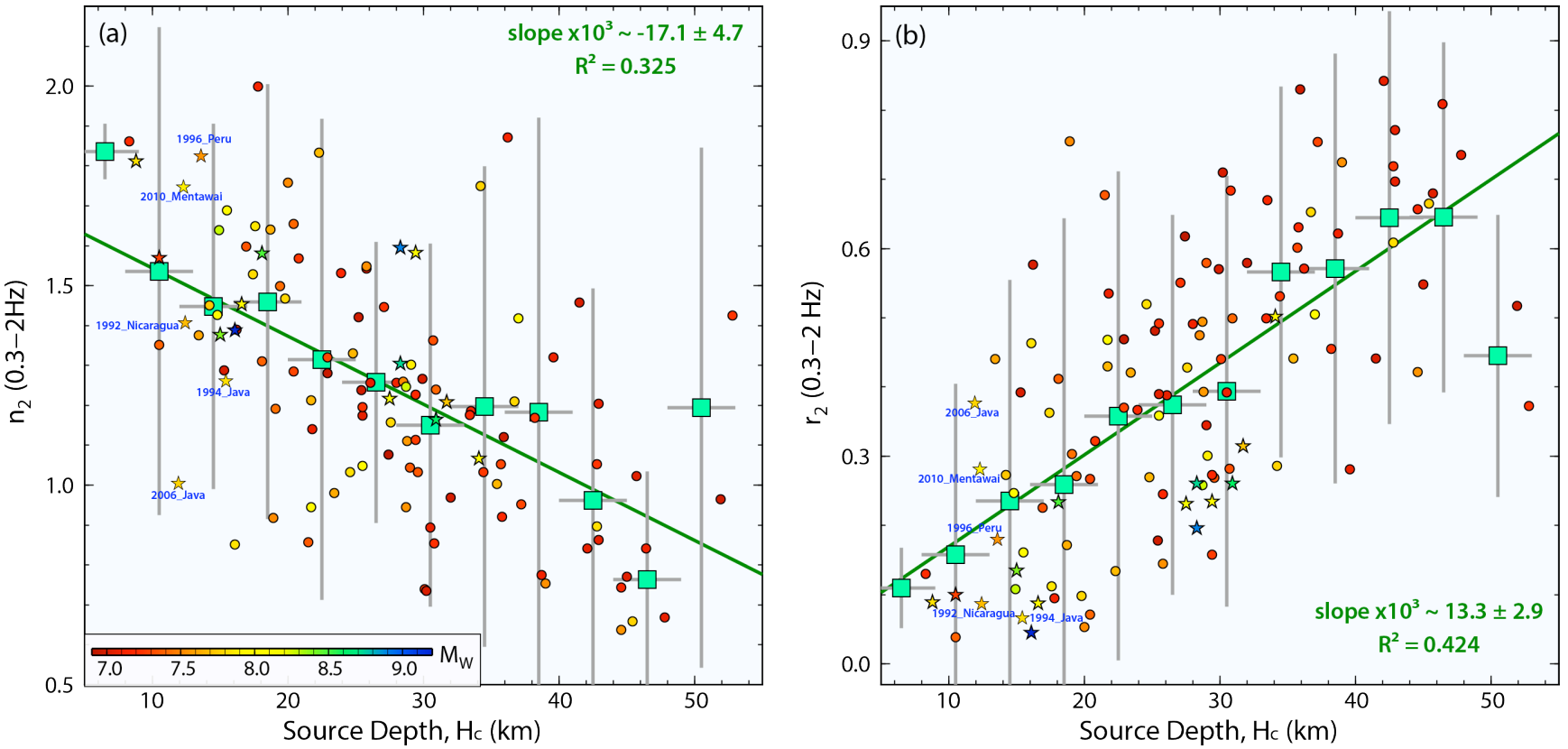

Figure S1. Regression slopes and correlation coefficients of the (a) 0.3-2 Hz spectral slop measures, and (b) ratios of high-frequency (0.3-2 Hz) radiated energy over total radiated energy, as functions of average depth of the slip distribution from the finite-fault source models. Colors of circles and stars denote M_w. The squares show the average value over each 5 km depth range as indicated by the horizontal gray lines. The vertical gray lines indicated the range of 2σ, where σ is the standard deviation. The coefficient of determination R^2 is shown for each case.

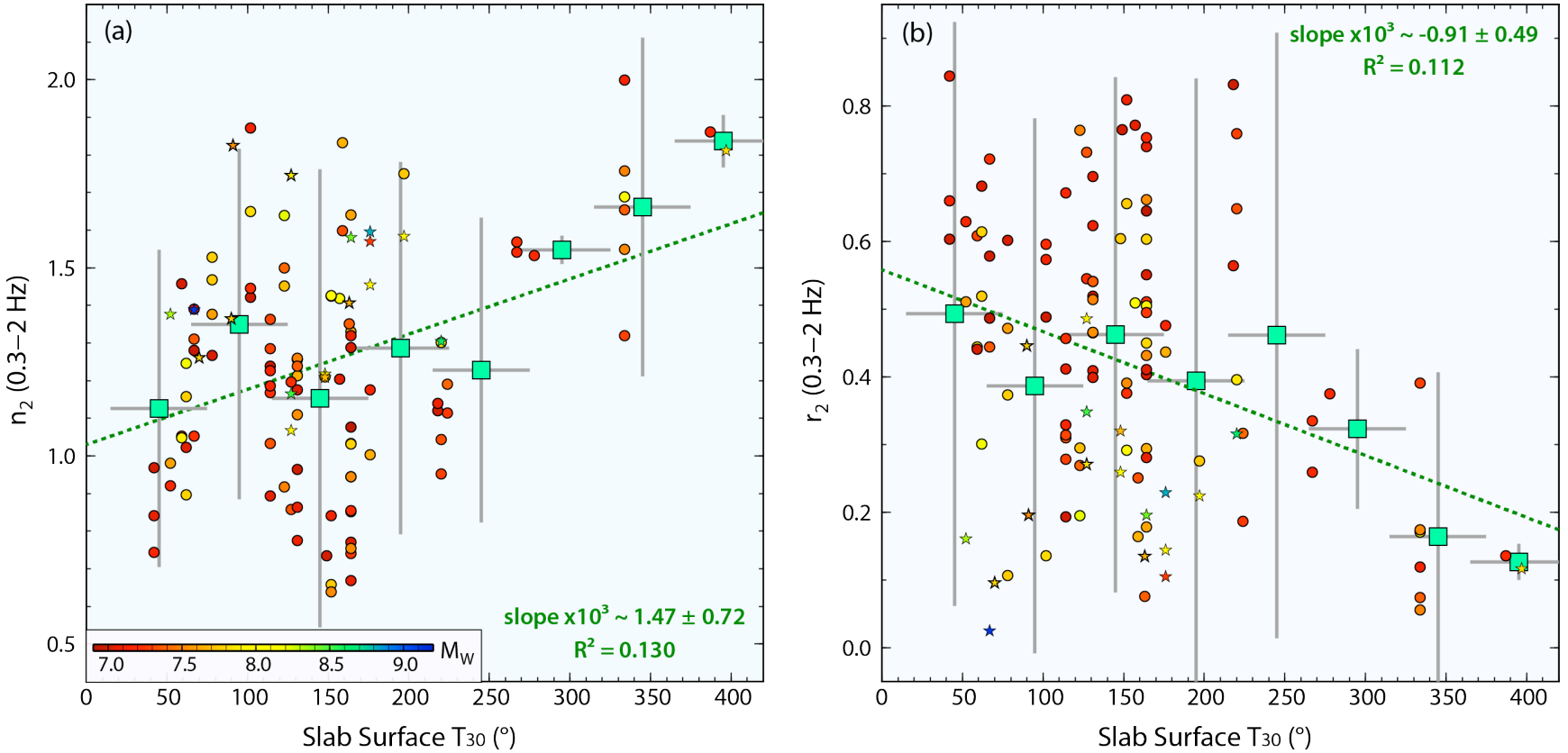

Figure S2. Regression slopes and correlation coefficients for the (a) 0.3-2 Hz spectral slope measures, and (b) ratios of high frequency (0.3-2 Hz) radiated energy over total radiated energy, as functions of estimates of surface temperature of the subducting slab at 30 km depth [Syracuse *et al*., 2010]. Symbols sizes are scaled with M_w from 7 to 9. The squares show the average value over each 50° range depth range as indicated by the horizontal gray lines. The vertical gray lines indicated the range of 2σ, where σ is he standard deviation. The coefficient of determination R^2 is shown for each case.

Description for supplementary file of regional faulting parameters.

Supplement S1. Finite-fault model information, source spectra, earthquake slip distributions versus depth, and source parameter relationships with depth for 17 regions sampled by out data set of 114 major and great earthquakes. For each region a first page shows the slip distributions from finite-fault inversions for events in that region are shown on a map with true relative placement of the slip and common slip scale. The average source spectra and spectral fitting parameters described in the text are shown for all events in each region, along with the distribution of slip and seismic momen versus depth for each event. The second page shows the depth distribution of scaled centroid time, moment-scaled radiated energy, apparent stress, stress drop from the variable slip finite-fault model, slopes of the high-frequency spectral amplitude curves, and the high-frequency/total radiated energy ratio. Dashed lines indicate the average values for the whole population for each parameter.